CHEMISTRY OF MATERIALS

Unravelling Ultraslow Lithium-Ion Diffusion in γ-LiAlO₂: Experiments with Tracers, Neutrons, and Charge Carriers

Dennis Wiedemann,*,[†] Suliman Nakhal,[†] Johanna Rahn,[‡] Elena Witt,[§,∥] Mazharul M. Islam,[⊥] Stefan Zander,[#] Paul Heitjans,[§,∥] Harald Schmidt,[‡,∥] Thomas Bredow,[⊥] Martin Wilkening,[¶] and Martin Lerch[†]

[†]Institut für Chemie, Technische Universität Berlin, 10623 Berlin, Germany

[‡]Institut für Metallurgie, Technische Universität Clausthal, 38678 Clausthal-Zellerfeld, Germany

[§]Institut für Physikalische Chemie und Elektrochemie, and [∥]ZFM−Zentrum für Festkörperchemie und Neue Materialien, Leibniz Universität Hannover, 30167 Hannover, Germany

[⊥]Mulliken Center for Theoretical Chemistry, Universität Bonn, 53115 Bonn, Germany

[#]Abteilung Kristallographie, Helmholtz-Zentrum Berlin für Materialien und Energie, 14109 Berlin, Germany

[¶]Institut für Chemische Technologie von Materialien, Christian Doppler Laboratory for Lithium Batteries, Technische Universität Graz, 8010 Graz, Austria

S *Supporting Information*

ABSTRACT: Lithium aluminum oxide (γ-LiAlO₂) has been discussed and used for various applications, e.g., as electrode coating, membrane, or tritium breeder material. Although lithium-ion diffusion in this solid is essential for these purposes, it is still not sufficiently understood on the microscopic scale. Herein, we not only summarize and assess the available studies on diffusion in different crystalline forms of γ-LiAlO₂, but also complement them with tracer-diffusion experiments on (001)- and conductivity spectroscopy on (100)-oriented single crystals, yielding activation energies of 1.20(5) and 1.12(1) eV, respectively. Scrutinous crystal-chemical considerations, Voronoi−Dirichlet partitioning, and Hirshfeld surface analysis are employed to identify possible diffusion pathways. The one-particle potential, as derived from high-temperature powder neutron diffraction data presented as well, reveals the major path to be strongly curved and to run between adjacent lithium positions with a migration barrier of 0.72(5) eV. This finding is substantiated by comparison with recently published computational results. For the first time, a complete model for lithium-ion diffusion in γ-LiAlO₂, consistent with all available data, is presented.
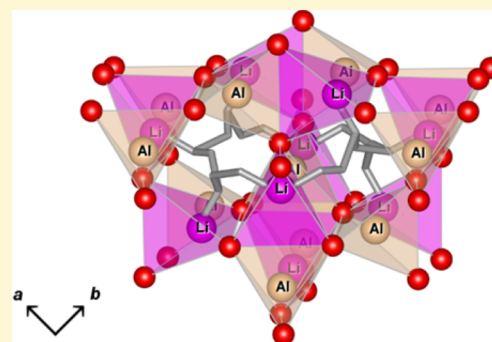
INTRODUCTION

For more than three decades, γ-LiAlO₂ has been discussed for or implemented in a broad variety of applications: as a coating for lithium-conducting electrodes,[1,2] as an additive in composite electrolytes,[3] as a template for epitaxial growth of III−V semiconductors,[4] as a membrane material for molten-carbonate fuel cells,[5] and as a tritium-breeder material in fusion reactors.[6,7] Despite being the crucial process for these purposes, lithium diffusion in this poor ion conductor is not yet fully understood on the microscopic scale.

Six polymorphs of lithium aluminum oxide have been announced so far: hexagonal α- ($R\bar{3}m$, NaCrS₂ type), orthorhombic β- ($Pna2_1$, β-NaFeO₂ type), tetragonal γ- ($P4_12_12/P4_32_12$, γ-LiAlO₂ type), tetragonal δ- ($I4_1/amd$, α-LiFeO₂ type), cubic ε-LiAlO₂ ($I4_132$, structure unknown), and a dubitable monoclinic phase ($P2/m$, structure unknown).[8] Among these, only the structures of the α-,[9] γ-,[10,11] and δ-phase[12] have been soundly established using diffraction

techniques. Being the most stable form under ambient conditions, γ-LiAlO₂ was discovered by Weyberg in 1906,[13] but its powder X-ray diffractogram had not been indexed before 1951.[14] In 1965, the structure was finally elucidated using powder neutron and single-crystal X-ray techniques.[10,11]

In γ-LiAlO₂, distorted MO₄ tetrahedra (M = Al, Li) form a three-dimensional network. Each tetrahedron shares one edge with a tetrahedron containing a metal ion of the other sort. In these pairs, each vertex is shared with two additional tetrahedra, one of each kind. This topology gives rise to small, roughly hexagonal channels along the ⟨100⟩ directions and larger, roughly quadrangular channels along [001] (see Figure 1). Voids constitute the latter by forming two interpenetrating chains of empty, strongly distorted edge-sharing octahedra
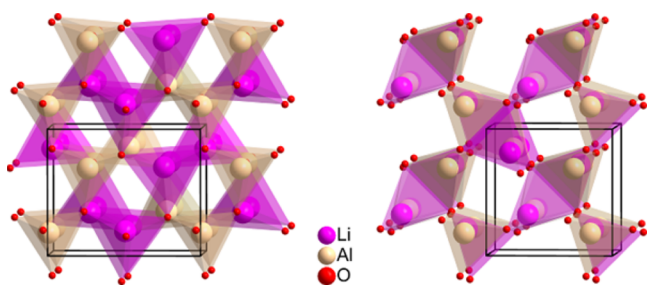
Figure 1. Crystal structure of γ-LiAlO₂ with view approximately along [100] (left) and [001] (right); unit cell in black.

(type A). Alternatingly, less distorted ones (type B) share faces with the type-A voids along ⟨100⟩ and give rise to the hexangular channels.

Since the 1980s, several experimental studies have dealt with lithium-ion migration in γ-LiAlO₂, associated jump rates, diffusivities, and activation barriers (see Table 1). The methods of choice have mainly been conductivity spectroscopy (CS) and

Table 1. Activation Energies E_A for Lithium-Ion Migration in γ-LiAlO₂

T (K)	method	E_A (eV)	ref.
experimental			
polycrystalline (unspecified)			
705−903	NMR (T_1)	0.77	15
773−823	NMR (MN)[a]	0.81	23
N/A	CS	0.79 (extrinsic)[b]	15
723−1036	CS	0.81 (extrinsic)[b]	23
1036−1135	CS	1.26 (intrinsic)[b]	23
N/A	CS	1.47 (intrinsic)[b]	15
microcrystalline			
78−873	Raman spectroscopy	0.5−0.8	17
298−973	NMR (various)[c]	0.7	24
680−870	CS	0.9	24
473−573	CS	1.17[d]	20
nanocrystalline			
353−573	CS	0.96[d]	20
single-crystalline, [110]			
700−1000	NMR (T_1)	0.7	25
773−1023	NMR (T_1)	0.72(2)	16
553−923	NMR (MN)[a]	0.96(2)	16
673−923	NMR (quad. sat.)[e]	1.12(1)	16
423−603	CS	1.14(1)	16
single-crystalline, [001]			
423−603	CS	1.26(1)	16
single-crystalline, [100]			
293−533	CS	1.22(1)	26
533−1048	CS	1.12(1)	26
446−512	DMA[f]	1.2(1)	26
393−823	electric modulus	1.02−1.12	26
computational			
600−1200	MD	0.52	22
0	cNEB	0.64−1.71	21

[a]Motional narrowing of central transition. [b]Transition between extrinsic and intrinsic region at T_{tr} = 1036 K. [c]Spin−lattice relaxation in the laboratory (T_1) and rotating frame ($T_{1\rho}$), decay of spin-alignment echoes (SAE). [d]Extrema for pure phases during gradual high-energy ball milling. [e]Coalescence of quadrupolar satellites. [f]Dynamic mechanical analysis.

nuclear magnetic resonance (NMR) techniques. Unfortunately, these have not given fundamental insight into the actual migration pathways, although some characteristics have been proposed: The lower activation barriers (0.7−0.8 eV) have been attributed to a process involving extrinsic defects generated by impurities, the higher ones (1.0−1.3 eV) to a process involving intrinsic defects generated at higher temperature.[15] Indris et al. assumed that the lower barrier, as monitored by ⁷Li NMR spin−lattice (T_1) relaxation, is due to correlated lithium-ion movement via a vacancy mechanism. The actual jump path may be longer than the distance to the nearest lithium site and comprise interstitial positions or channels, leading to a complex dependence of the activation barrier extracted from the low-temperature flank of the diffusion-induced $1/T_1$ (T) peak.[16] On the basis of Raman spectroscopy, the movement of a lithium ion from its coordination tetrahedron to a vacant site or interstitial position has been proposed.[17] This suggestion has been substantiated by results of single-crystal neutron diffraction hinting at a strongly curved migration pathway between adjacent lithium sites.[18] Finally, introducing defects by high-energy ball milling (under partial amorphization or transformation into the high-pressure α-/δ-phase) as well as amorphization by ion-beam sputtering[19] have been shown to decrease intrinsic activation energies. The generation of octahedral coordination sites, which are also present in the high-temperature phases, has been speculated to play a major role in these processes.[20] Recently, some of us performed a theoretical investigation of lithium-ion diffusion and obtained activation energies in the range of 0.64 to 1.71 eV depending on the local environment.[21] In an earlier molecular dynamics (MD) simulation, an activation barrier of only 0.52 eV was calculated for lithium self-diffusion in an ideal crystal.[22]

In this work, we extend the range of experimental methods by adding (macroscopic) tracer-diffusion measurements. Furthermore, we present a consistent model of actual lithium-ion diffusion pathways and their activation barriers based on results of high-temperature neutron diffraction.

■ MATERIALS AND METHODS

Syntheses. For the **tracer diffusion experiments**, about 20 nm thin isotope enriched [⁶Li]AlO₂ films were deposited on commercial (001)-oriented γ-LiAlO₂ single crystals (CrysTec, Berlin) as a tracer source by ion-beam sputtering. Sputtering was carried out using a commercial setup (IBC 681, Gatan) equipped with two penning ion sources. The deposition was done at 5 keV and at 220 μA in argon at an operation pressure of 5 × 10⁻⁵ mbar. The base pressure was better than 5 × 10⁻⁷ mbar. The sputter process was carried out at room temperature and no significant heating of the substrate took place.

Sputter targets were prepared by solid-state syntheses: In an agate mortar, coarse γ-Al₂O₃ (99.997%, Alfa Aesar) was pestled to a fine powder and mixed with enriched [⁶Li]₂CO₃ (95.56% ⁶Li, Eurisotop) or [⁷Li]₂CO₃ (99.94% ⁷Li, Eurisotop). After subsequent ball milling of the powder mixture in a "SPEX 8000M" shaker mill, pellets of 1.6 cm in diameter were pressed and heated to 973 K with a rate of 2 K min⁻¹. The reaction step was followed by a sintering process at 1173 K for 12 h, which yielded polycrystalline dense targets. In order to account for loss of lithium in the sputtering process, the molar ratio of oxide and carbonate was chosen as 5:6.

For the diffusion experiments, the single crystals with tracer layer on top were annealed in an argon atmosphere using a commercial rapid-annealing setup (AO 500, MBE, Germany).

γ-LiAlO₂ powder for diffraction was prepared at 1373 K by a solid-state reaction. Li₂CO₃ (99.997%, Aldrich) and α-Al₂O₃ (99.98%, Alfa Aesar) were used as starting materials in a molar ratio of 1:1. The powders were carefully mixed and pressed into pellets. The samples

were then slowly heated to 1373 K, annealed for 20 h and quenched in air by removing them quickly from the furnace.

The oxygen content of the powder was confirmed using a "LECO EF-TC 300" N_2/O_2 analyzer (hot-gas extraction). Phase purity was confirmed by inspection of X-ray diffractograms recorded on a "PANalytical X'Pert PRO MPD" powder diffractometer in Bragg−Brentano (θ−θ) geometry equipped with Cu-K_α source and a "PIXcel" detector.

Tracer Diffusion. Secondary-ion mass spectrometry (SIMS) investigations in depth profile mode on the [^{6}Li]AlO$_2$-coated single crystals were carried out using a "Cameca ims 3f/4f" machine. Due to electrical charging during the measurements, we used an O$^-$ primary ion beam (15 keV, 50 nA). The sputtering area was of $250 \times 250\ \mu m^2$. For analysis of the isotopes in a double-focused mass spectrometer, the signal resulting from an area of about $60 \times 60\ \mu m^2$ in the center of the sputtering area was used to exclude crater-edge effects.

The secondary ion intensities of the two lithium isotopes, $I(^6Li^+)$ and $I(^7Li^+)$, were recorded as a function of sputter time in depth-profiling mode. Since the two lithium isotopes are chemically identical (neglecting the small isotope effect), for diffusion analysis, the intensity of the signals was converted into ^{6}Li atomic fractions c according to the following:

$$c = \frac{I(^6Li^+)}{I(^6Li^+) + I(^7Li^+)} \tag{1}$$

Depth calibration of each sputter crater was realized by measuring the depth with a mechanical profilometer (Tencor, Alphastep).

Conductivity Spectroscopy. γ-LiAlO$_2$ single crystals were purchased from CrysTec (Berlin, Germany). For the experiments carried out at lower temperatures, silver conductive adhesive paste and platinum sheets (both Alfa Aesar) were used to apply electrodes on both polished sides of the wafer. Conductivity isotherms were recorded from 293 K on a "Novocontrol Concept 41" system ("Alpha-A" analyzer, active ZGS cell, "Novocool" cryosystem). Measurements were performed in dinitrogen atmosphere. The conductivity measurements carried out at higher temperatures are described elsewhere.[26]

Powder Neutron Diffraction. Measurements were carried out at the FIREPOD instrument (E9) with Ge(511)-monochromated neutrons (λ = 179.82[1] pm) in Debye−Scherrer geometry at *Helmholtz-Zentrum Berlin für Materialien and Energie* (HZB, Germany). The compacted powder samples were mounted in a vacuum high-temperature furnace inside a tantalum cylinder (d = 9.7 mm, h = 55 mm). Measurements were carried out at 345−1777 K with exposure times of several hours. Data were recorded with an array of eight "DENEX" ^{3}He-counter area-detectors yielding a final range of 0° $\leq 2\theta \leq 142°$ with $\Delta(2\theta)$ = 0.075°. At very high temperature, reflections of α-LiAlO$_2$ appeared, showing the presence of ca. 1% and 3% of this material at 1676 and 1777 K, respectively. Table 2 lists further experimental details.

For Rietveld refinement, a model was imported from the Inorganic Crystal Structure Database (ICSD)[27] and refined with JANA2006 against net intensities analytically corrected for absorption (cylindrical sample) using the full-matrix least-squares algorithm with fixed elements per cycle.[28] Regions containing the very strong reflections of the tantalum container were excluded from the refinement leaving a complex background, which was defined manually with 36−42 points interpolated using ten Legendre polynomials with refined coefficients. Peak profiles were fitted with a pseudo-Voigt function following the Thompson−Cox−Hastings approach.[29] Asymmetry was corrected for using the two-term Bérar−Baldinozzi method.[30]

All atoms were refined with anisotropic atomic displacement parameters, although $B_{13} = -B_{23}$ had to be set to zero for the very static aluminum ion at 345 K. Additionally, the lithium atom was modeled anharmonically with terms up to the order of four. With the exception of $D_{1112} = D_{1222}$ at 1475 K, which proved to be vital for a good fit, only statistically meaningful tensorial coefficients ($\geq 3\sigma$) were kept in the refinement. Because of strong correlation, B_{12}, D_{1113}, and

Table 2. Details of Neutron Powder Diffraction on γ-LiAlO$_2$

T (K)	345	1023	1475
crystal system	tetragonal	tetragonal	tetragonal
space group	$P4_12_12$	$P4_12_12$	$P4_12_12$
a/pm	515.885(17)	519.65(2)	522.52(2)
c/pm	627.00(3)	634.64(3)	640.38(3)
$V/10^6$ pm^3	166.868(10)	171.376(12)	174.843(12)
ρ_{calc}/g cm^{-3}	2.624	2.5549	2.5043
μ/mm^{-1}	0.170	0.165	0.162
$2\theta_{max}$/°	139.43	138.23	136.43
Data, constr., parameters	82, 1, 36	89, 0, 40	88, 0, 44
R_F (obs,[a] all)	0.0177, 0.0210	0.0136, 0.0199	0.0115, 0.0167
R_B (obs,[a] all)	0.0280, 0.0304	0.0196, 0.0247	0.0160, 0.0179
S (all)	1.39	1.15	1.20
wR_p, wR_{exp}[b]	0.0396, 0.0285	0.0321, 0.0278	0.0272, 0.0227
ρ_{min}, ρ_{max}/ 10^{-6} fm pm^{-3}	0.11, − 0.11	0.28, − 0.27	0.03, − 0.03
CSD No.	430357	430358	430359

[a]$I > 3\sigma(I)$. [b]$w = 1/[\sigma^2(F_0) + (0.01F_0)^2]$.

D_{3333} were fixed at the final stage for appropriate probability-density function (PDF) error estimation.

Structure graphics were produced using Diamond 3.2.[31] Analysis of the Hirshfeld surface under exclusion of lithium ions was performed using CrystalExplorer 3.1.[32] For Voronoi−Dirichlet partitioning analysis, Topos Pro 5.0[33] was employed in a standard procedure: After detection, too small elementary voids (spherical-domain radius $R_{sd} < 138$ pm for lithium ions in oxide environments) and channels (adjacency radius $R_{ad} < 180$ pm, 90% of typical Li−O distance) as well as those not only determined by oxide ions (solid angle of interaction with aluminum ions $\Omega > 10\% \times 4\pi$) were discarded.[34]

Maps of the PDF illustrating time- and space-averaged atomic distributions were generated within JANA2006. Assuming independent single-particle motion governed by Boltzmann statistics, effective one-particle potential (OPP) barriers were calculated using the facilities of JANA2006, which include a Monte−Carlo method for error handling (10 000 iterations).[35] Maps for visualization were created with the in-house program CalcOPP 1.6.1.[36] Results were visualized using VESTA 3.3 (isosurfaces)[37] and OriginPro 2015 (plots).[38]

RESULTS AND DISCUSSION

Tracer Diffusion. To gain access to the macroscopic diffusion behavior in γ-LiAlO$_2$, we have investigated lithium self-diffusion in (001)-oriented single crystals between 473 and 723 K using SIMS. A thin layer of ion-beam sputtered ^{6}Li-enriched lithium aluminum oxide has been used as a tracer source.

In Figure 2, a characteristic example for the ^{6}Li atomic fraction c as a function of the sputter depth x as derived from SIMS measurements is given. During annealing for a time t, the ^{6}Li tracer penetrates the single crystal up to a characteristic diffusion length (usually several hundred nanometers). The tracer diffusivity is then determined using standard procedures: Depth profiles after diffusion annealing are fitted by a solution of Fick's second law for self-diffusion across an interface (thin-film solution, see eq 2),[39] in which c_0 is the background ^{6}Li atomic fraction. The tracer diffusivity D^T and the measure M for the amount of diffusing species are treated as fit parameters.

$$c = c_0 + \frac{M}{\sqrt{\pi D^T t}} \exp\left(-\frac{x^2}{4D^T t}\right) \tag{2}$$

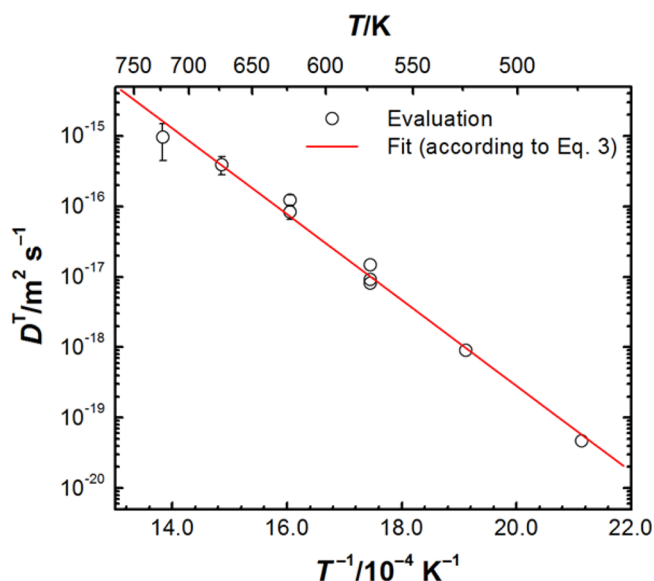In this case, a diffusivity of $D^T = 10(5) \times 10^{-16}$ m^2 s^{-1} is derived.
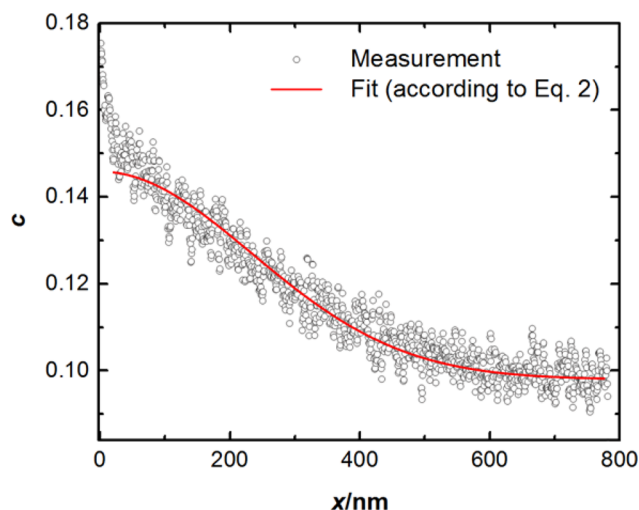
Figure 2. ^{6}Li atomic fraction c as a function of the sputter depth x for a sample annealed at 723 K for 28 s.

In Figure 3, the lithium tracer diffusivities determined in this way are plotted as a function of reciprocal temperature. They

Figure 3. ^{6}Li tracer diffusivities D^T in (001)-oriented γ-LiAlO$_2$ single crystals as a function of reciprocal temperature T^{-1} as obtained by SIMS.

obey the Arrhenius law (k_B: Boltzmann constant, T: temperature)

$$D^T = D_0^T \exp\left(-\frac{E_A}{k_B T}\right) \tag{3}$$

with an activation energy of $E_A = 1.20(5)$ eV and a pre-exponential factor of $D_0^T = 4.2^{+6.6}_{-2.6} \times 10^{-7} \mathrm{m^2 s^{-1}}$. Both quantities show values in the range of those known from other transition metal oxides.

Conductivity Spectroscopy. The Arrhenius activation energy for self-diffusion along [001] measured with tracer diffusion agrees very well with those derived from CS (see Table 1). Thus, both macroscopic techniques are sensitive to

the same dynamic process almost independent of the orientation of the crystal.

To complement the available data with respect to crystal orientation and temperature range, we have monitored long-range lithium transport in a (100)-oriented γ-LiAlO$_2$ crystal using CS in the low-temperature (LT) regime. Corresponding data in the high-temperature (HT) regime have been taken from literature.[26] The isotherms recorded (real part of conductivity vs frequency, see Figures S1 and S2) are dominated by frequency-independent plateaus. The corresponding direct-current (DC) conductivities σ_{DC} clearly refer to long-range ion transport. Since lithium ions are the only effective charge carriers,[23] the Nernst−Einstein relation was applied for the calculation of the solid-state diffusion coefficient D^σ, assuming that the number density of charge carriers is given by the lithium-ion concentration (n: number density of mobile carriers, q: electrical charge):

$$D^\sigma = \sigma_{DC} \frac{k_B T}{n q^2} \tag{4}$$

As depicted in Figure 4, the values thus obtained obey the same Arrhenius law throughout the whole temperature interval:
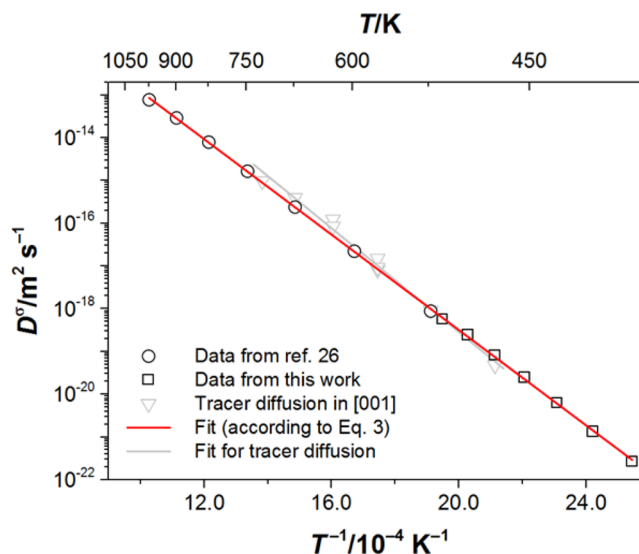
Figure 4. Solid-state diffusion coefficients D^σ in (100)-oriented γ-LiAlO$_2$ single crystals as a function of reciprocal temperature T^{-1} as obtained from DC conductivities σ_{DC} (D^T from tracer diffusion in gray for comparison; HT data taken from ref 26).

an overall activation energy of 1.12(1) eV is found. The tracer diffusion coefficients D^T are shown for comparison. Since the diffusion coefficients, D^T and D^σ, are related via the Haven ratio H_R, $D^T = H_R D^\sigma$, it seems to be close to 1. $H_R \approx 1$ serves as an indication that, indeed, lithium is the only mobile species in γ-LiAlO$_2$ and that strong correlation effects are absent. For comparison, Debye-like ion transport was found for γ-LiAlO$_2$ single crystals by means of both electrical impedance spectroscopy and mechanical loss analysis, quite recently.[26]

Combined with the available CS data from literature (see Table 1), these findings give rise to the following three conclusions:

- Long-range diffusion is essentially the same throughout the whole temperature range.

- Taking into account different crystal orientations, no pronounced anisotropy of the activation energy is found. The same mechanism may be the cause for movement in all the examined crystallographic directions.
- The lower activation energies found for poly-, micro-, and nanocrystalline materials using conductivity spectroscopy at lower temperatures are indeed due to extrinsically generated defects. In single crystals, only (scarce) intrinsic defects play a major role, thus, leading to higher barriers.

Nuclear Magnetic Resonance. Although this work includes no NMR studies, we want to shortly discuss the information on lithium diffusion, which has already been provided (cf. Table 1), from an atomic point of view. In particular, activation barriers of ca. 0.7 eV have been derived for single- and polycrystalline samples from the temperature-dependent, diffusion-induced spin−lattice relaxation times (T_1, $T_{1\rho}$). These were obtained from the low-temperature flank of the peaks in semilogarithmic plots of T_1^{-1} against the inverse temperature. As is well-known,[40] the low-temperature flank yields activation energies for local lithium jumps, which are generally expected to be lower than those obtained from the high-temperature flank of the $1/T_1$ peak or DC conductivity data. Both represent long-range lithium ion motion.

Motional narrowing (MN) of the line width has been used to estimate activation barriers of 0.81−0.96 eV in single- and polycrystalline samples. Both the dipolar and the quadrupolar contributions to the NMR line shape get averaged upon heating, but the extent of averaging of each may be different.[41] Since one can use different fitting approaches for MN data, the obtained activation energies can have certain deviations and should be viewed as rough approximations.[42] A similar value of 1.12(1) eV has been deduced from the coalescence of quadrupolar satellites. Due to the different time scales of the latter methods, these results may also reflect the long-range lithium motion. Thus, taken with a pinch of salt, the data listed in Table 1 do not contradict our findings from tracer-diffusion and conductivity measurements.

Topological Analysis. After the initial characterization, we were interested in mapping the pathways of ultraslow diffusion in crystalline γ-LiAlO$_2$ experimentally. As heuristic approaches, we have chosen crystal-chemical considerations, the Voronoi−Dirichlet partitioning and the Hirshfeld surface analysis of the AlO$_2^-$ framework to examine the void structure topologically. The latter two methods have already proven their value for battery materials and fast ion conductors.[34,43]

First, we have had a closer look at approximated crystal voids and their interconnection. In addition to the channels mentioned in the introduction, the voids of type B form chains of edge-sharing octahedra along [100]. The face-sharing tetrahedra in between them are, however, alternatingly filled with lithium and aluminum ions, thus, making them unavailable for migration. Geometrical data (see Table S1) show that voids of type B are less strongly distorted from ideal octahedra than those of type A, have nearly ideal center−oxide distances for lithium ions ($d_{\mathrm{eff}}[\mathrm{Li^+_{IV}}-\mathrm{O^{2-}_{IV}}]$ = 214 pm,[44] $\bar{d}$[B−O] = 216 pm), but exhibit by ca. 10 pm shorter average distances to adjacent cations. This possibly makes them more appropriate for hosting interstitial, but less fit for conducting migrating lithium ions (cf. Computational Methods).
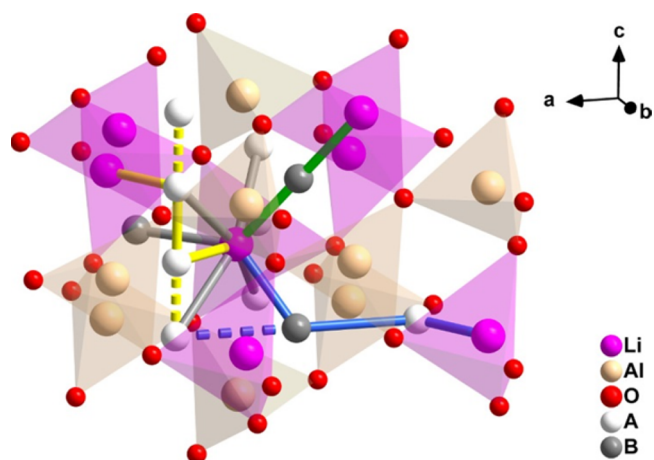
At room temperature, the distances between a lithium reference position (Li) and the nearest (Li′), second (Li″) and

third nearest one (Li‴) are 308.3(5), 418.5(4), and 489.0(5) pm, respectively. The possible elementary jump processes (up to a distance of 350 pm) are listed and assessed in Table 3.

Table 3. Elementary Jumps in γ-LiAlO$_2$ at Room Temperature (Rejected Ones in Italics)

jump	d (pm)	description
Li ⇌ A	188	through center of LiO$_4$ face
Li ⇌ B	209	through center of LiO$_4$ face
A ⇌ A′	156	along large channels in [001]
A ⇌ B	258	along small channels in ⟨100⟩
Li ⇌ A′	*244*	*through LiO$_4$ face under a very acute angle*
Li ⇌ B′	*226*	*through center of a tetrahedron edge*
Li ⇌ Li′	*308*	*through center of a LiO$_4$ edge, through LiO$_4$ face under a very acute angle*
A ⇌ B′	*302*	*grazing AlO$_4$ edge along ⟨201⟩*
B ⇌ B′	*313*	*through center of a shared AlO$_4$/LiO$_4$ edge, along [001]*

Those, that are crystal-chemically disfavored, have been rejected. The remainder was used to construct the following possible pathways between lithium positions (see Figure 5):

$$\mathrm{Li} \rightarrow \mathrm{A} \rightarrow \mathrm{A'} \rightarrow \mathrm{Li'} \qquad \qquad (\mathrm{P1})$$

$$\mathrm{Li} \rightarrow \mathrm{B} \rightarrow \mathrm{Li''} \qquad \qquad (\mathrm{P2})$$

$$\mathrm{Li} \rightarrow \mathrm{A} \rightarrow \mathrm{B} \rightarrow \mathrm{Li'''} \qquad \qquad (\mathrm{P3})$$

Figure 5. Proposed lithium diffusion pathways in γ-LiAlO$_2$ (yellow: P$_1$, green: P$_2$, blue: P$_3$, gray: disfavored jumps; dashed lines: possible infinite expansions).

P$_1$ and P$_3$ are strongly curved and may be infinitely expanded by including more A or A/B sites (i.e., migration in a channel along [001] or ⟨100⟩, respectively), whereas P$_2$ is strictly linear and finite. The sheer length of P$_3$ and the large A−B distance make this path much less probable.

We have also subjected the structural model to Voronoi−Dirichlet partitioning of the AlO$_2^-$ substructure according to the standard procedure as a more sophisticated method taking into account the size and nature of a migrating ion (see Figure 6).

The conduction pattern comprises the actual lithium positions as largest elementary voids. These are connected to their neighbors by significant elementary channels that coincide with P$_1$, but exhibit more features and segments. The elementary channels branch into the quadrangular crystal
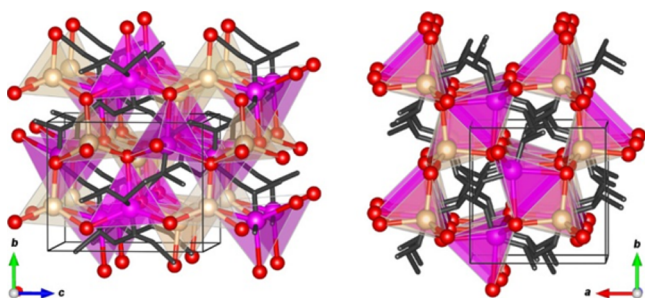
Figure 6. Conduction pattern of γ-LiAlO$_2$ according to Voronoi−Dirichlet partitioning analysis with view approximately along [100] (left) and [001] (right); black: lithium-accessible elementary voids/channels, pink: lithium ions, ocher: aluminum ions, red: oxide ions; unit cell in black.

channels along [001] (see Figure 6, right), suggesting possible migration excluding the lithium positions (i.e., successive A → A′ → A″ jumps). The same feature may allow for conduction along ⟨100⟩ on helical pathways comprising two adjacent hexangular crystal channels (see Figure 6, left). It is noteworthy that the pathway is strongly curved and neither of the B-containing paths P$_2$ and P$_3$ is reproduced—nor is any other type of elementary jump.

As another topological method, the analysis of the crystal void surface of the AlO$_2^-$ framework (see Figure S3) corroborates the findings from the Voronoi−Dirichlet partitioning. The helical pathway along [001], giving also rise to the lithium-position comprising helix along ⟨100⟩, is clearly discernible. The void surface connects to a 3D network at an isovalue of 0.0045 × 10^{-6} e pm^{-3}, which is in the typical range for closely packed structures.

Neutron Diffraction. Having an idea of the possible diffusion pathways, we wanted to acquire quantitative data, i.e., to learn about their potential barriers. For this purpose, neutron diffraction is an ideal tool: It yields high-resolution structural—albeit time- and space-averaged—data and is, in contrast to X-ray diffraction, sensitive for light elements like lithium. From the data, a model may then be derived that contains information about the distribution of the lithium ions in the Debye−Waller factor (DWF). The inclusion of anharmonic terms in its description, e.g., using the Gram−Charlier expansion, grants models beyond the spherical (harmonic-isotropic) or ellipsoidal (harmonic-anisotropic) approximations.[45] This enables the derivation of an accurate PDF $F(\boldsymbol{u})$, describing the differential probability for the presence of a lithium ion in a given volume element. The PDF, on its part, allows for the calculation of an effective OPP $V(\boldsymbol{u})$ as experienced by an average lithium ion ($\boldsymbol{u}$: displacement from the reference position):

$$V(\boldsymbol{u}) = -kT\ln\left[\frac{F(\boldsymbol{u})}{F_{\max}}\right]$$

(5)

In this approach, every ion is treated as an individual Einstein oscillator subject to Boltzmann statistics in the classical limit [$kT \gg V(\boldsymbol{u})$]. The maximum of the OPP along a certain path is the migration activation energy E_m, *not comprising the defect formation energy*.[46]

The relatively short duration of powder neutron diffraction allowed us to collect temperature-dependent data from 345 up to 1777 K. In this range, the directional and volumetric thermal expansions behave linearly without anomalies (cf. Figure S4).

The data acquired at 345 and 1023 K (see Table 2 and Figure S5−S6) compare very well to those from the single-crystal measurements published before:[18] A split lithium position is not found at the lower temperature, but sets in at the higher one, being very much in tune with the transition from the extrinsic to the intrinsic region at T_{tr} = 1036 K. The available high-angle diffraction data allowed for the modeling of the lithium ion including anharmonic terms at the reference position (x, x, 0).

To get reliable information about the diffusion pathways, it is however necessary to evaluate the behavior at a temperature high enough to warrant a sufficient migration. As the effects of a transformation to α-LiAlO$_2$ altered the diffractograms from 1575 K up, we have chosen the data set from the experiment at 1475 K (cf. Figure S7) for this purpose. In the course of Rietveld refinement, successively more parameters were added to describe the lithium DWF (harmonic-isotropic → harmonic-anisotropic → third order anharmonic → fourth order anharmonic). Fourier-synthesis maps of the observed scattering-length density showed two separate minima close to the lithium reference position. However, refinements with the ion at a general position under symmetry breaking introduced too many intensity-dependent parameters. Nonetheless, the final model correctly describes the minima by means of higher order DWF terms. Remarkably, but not uncommonly, the anharmonic model did not significantly improve the fit before adding terms of the fourth order (cf. Table S2, Figures S8 and S9). A glance at the Figure 7 sheds light on this matter: Only the
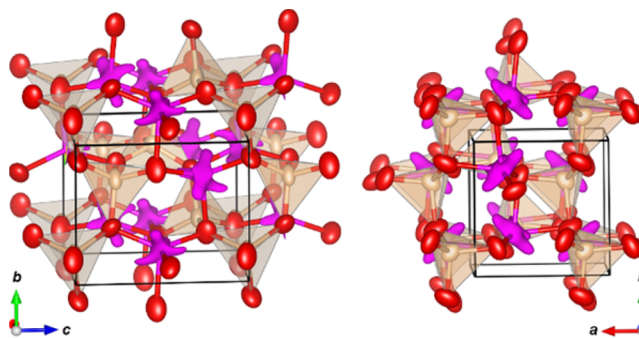
Figure 7. Lithium PDF and crystal structure at 1475 K as derived from powder neutron diffraction data with view approximately along [100] (left) and [001] (right); pink: isosurface for probability density of 0.75 × 10^{-6} pm^{-3}, ocher: aluminum ions, red: oxide ions with ellipsoids of 75% probability; unit cell in black.

higher-order terms allow for modeling of arm-like structures stretching out into the channels toward neighboring lithium positions—just as hinted at by the topological methods.

By searching the vicinity of straight connections, we have evaluated slightly curved pathways of minimal OPP for the probable elementary jumps and for the direct jump from one lithium position to an adjacent one (see Table 4). The optimal (lowest migration barrier) path between neighboring lithium ions is strongly curved in two dimensions, traverses a type-A void, but does not include its center (see Figure 8). This is consistent with the path that has been estimated on the basis of single-crystal neutron diffraction before.[18] Judging from the high and uncertain migration energies of jumps including type-B voids, these may not be part of actual pathways (thus, excluding P$_2$ and P$_3$). Nearly straight jumps between two adjacent lithium sites seem possible, but are disfavored in

Table 4. OPP-Derived Migration Barriers E_m for Different Jumps in γ-LiAlO$_2$ at 1475 K

jump	E_m (eV)	position of maximum
Li $\rightleftarrows$ A	0.87(4)	(0.50, 0.00, 0.00), center of type-A void
Li $\rightleftarrows$ B	2.55(48)	(0.45, 0.45, 0.01), near center of type-B void
A $\rightleftarrows$ A′	1.28(13)	(0.56, 0.06, 0.46), near center of type-A void
A $\rightleftarrows$ B	2.63(98)	(0.50, 0.50, 0.00), center of type-B void
Li $\rightleftarrows$ Li′	1.06(25)	(0.79, 0.54, 0.14), on LiO$_4$ edge
optimal	0.72(5)	(0.42, 0.15, 0.28), inside type-A void

comparison with the optimal curved path. Although P$_1$ has a markedly higher migration barrier (with A $\rightleftarrows$ A′ being the limiting step), it must be taken into account as a possible minor pathway. The method of evaluation suffers from overestimating barriers far away from reference positions (i.e., near the void centers).

Bearing this in mind, the found paths agree well with those proposed by topological considerations even if they are not superimposable (the latter fact is due to the void analyses not considering any attractive or repulsive electronic effects, but rather the atoms' spatial arrangement only). Direct jumps on curved paths make up the major, migration along the channels in [001] a possible minor mechanism.

The migration barrier for the former allows estimating the formation energy E_f for mobile defects: $E_f = E_A - E_m \approx 1.20$ eV $- 0.72$ eV $= 0.48$ eV. This value seems very low in comparison to, e.g., the 2.53/2.12 eV (measured/calculated) for lithium Frenkel-defect formation in Li$_2$O.[47] For γ-LiAlO$_2$, energies of the same magnitude would be expected, so that a Frenkel mechanism can be ruled out in this case. Our low assessed value may be due to preformation at boundaries of polysynthetic growth twins by inversion, which are highly abundant in γ-LiAlO$_2$ crystals grown using the Czochralski method (like the ones used in our studies).[48,49] The energetics of lithium-ion transport in oxidic materials have already been shown to be substantially altered by the presence of twin boundaries, both

experimentally (for SnO$_2$ nanowires)[50] and computationally (e.g., for LiCoO$_2$).[51] In addition, a very recent analysis of the material's defect structure shows that lithium vacancies, introduced by transition-metal impurity ions on cation sites (e.g., by iron(II) on a lithium position), play a major role.[52] The authors of the study postulate that "large concentrations of these lithium vacancies are introduced into the crystal during growth." If this is indeed the case, then a low formation energy for mobile defects, as estimated by us, is to be expected.

Computational Methods. To rationalize our findings so far on a still more fundamental level, we have interpreted a computational investigation of various lithium diffusion pathways recently published by some of us in the framework of this study.[21]

Formally introduced by removing an electroneutral atom, lithium deletions cannot be abundant defects under ambient conditions, as they would require local formation of unstable oxygen(−I) species. Frenkel defects are more likely to occur and could, in contrast to impurity substitution, readily be modeled. Test calculations have shown that the placement of the interstitial lithium ion into type-B voids leads to more stable configurations than placing them into type-A voids—but only by a very small energy difference.

In the aforementioned study, lithium ions were made to migrate from their regular coordination tetrahedra to a first (Li′), second (Li″), or third (Li‴) nearest neighboring vacancy. In order to verify the effect of local defect structure on migration energies, the distances between the interstitial lithium ion, vacancy, and the migrating ion were varied. For Li $\rightleftarrows$ Li′/Li‴, the lowest migration barriers were found for the largest distances to the interstitial lithium ion (situated at a type-A site). For Li $\rightleftarrows$ Li″, the contrary proved to be valid. As a minimal effect on migration is expected with the interstitial lithium ion at the largest distance to the vacancy (thus, mimicking a vacancy introduced by impurity doping), Table 5 lists migration distances and barriers for these situations.
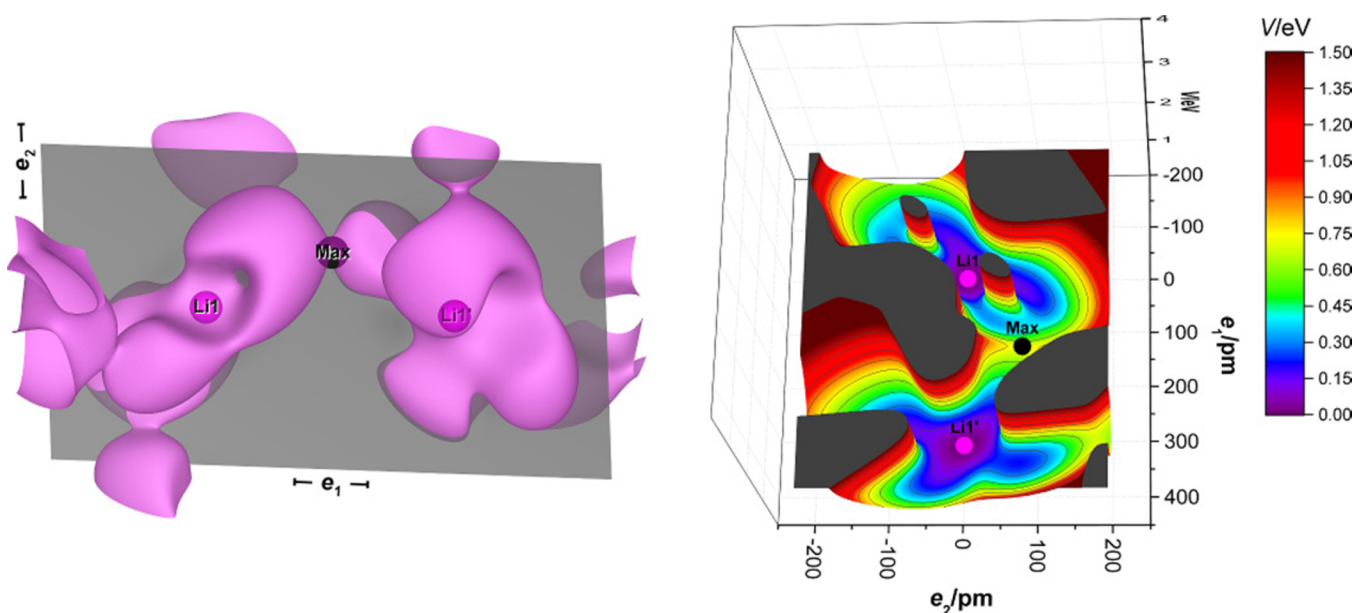
Figure 8. Optimal diffusion path between two adjacent lithium positions (pink: Li1, Li1′) and position of the OPP maximum (black: Max) at 1475 K. Left: PDF isosurface for lithium probability density of 0.0125×10^{-6} pm^{-3} (pink) with section through Li1, Li1′, and Max [gray, ca. (0 10 47)]. Right: 3D OPP map for the same section (e_1, e_2: orthogonal coordinates with origin at Li1; dark gray: areas of infinitely high potential).

Table 5. Calculated Migration Barriers E_m for Different Jumps in Frenkel-Defective γ-LiAlO$_2$ (d: Migration Distance, d_i: Distance from Vacancy to Interstitial; Data Taken from Ref 21)

path	d (pm)	E_m (eV)	d_i (pm)
Li $\rightleftarrows$ Li$'$	308	0.64	652
Li $\rightleftarrows$ B $\rightleftarrows$ Li$''$ (P$_2$)	414	1.71	504
Li $\rightleftarrows$ A$'$ $\rightleftarrows$ Li$'''$	488	1.45	651

The transition state (TS) for Li $\rightleftarrows$ Li$'$ corresponded to a distorted tetrahedron with two shorter (180 and 186 pm) and two larger (253 and 263 pm) Li—O distances (average for a regular tetrahedron: 200 pm). In this configuration, the migrating ion occupied the exact middle of a straight line connecting Li and Li$'$, bisecting an edge of the lithium coordination tetrahedron. This indicates a path equal to the experimentally investigated Li $\rightleftarrows$ Li$'$ jump with its OPP maximum coinciding with the aforementioned position. The computed migration barrier (0.64 eV) is reconcilable with the experimental one (1.06(25) eV). London dispersion was found to have a non-negligible effect on the calculated migration barriers. By means of Grimme's DFT-D3(BJ) correction,[53] the TS for Li $\rightleftarrows$ Li$'$ was recalculated. The barrier increased by 0.05 to 0.69 eV. Even though the optimal, strongly curved path with $E_m = 0.72(5)$ eV avoiding the crossing of a tetrahedron edge was not found by computation, it made clear that a direct jump from a lithium position to an adjacent vacancy is the energetically preferred migration process in γ-LiAlO$_2$.

Along the path Li $\rightleftarrows$ Li$''$, the migrating lithium ion passed through a distorted type-B octahedron to the nearest regular lithium site. In the TS, all the Li—O bonds were in the range of 200−220 pm. This path thus identifies as P$_2$; the TS lithium position roughly coincides with the experimental maximum position in a Li $\rightleftarrows$ B jump. With 2.55(48) eV/1.71 eV, the experimental and computed migration barriers are reconcilable. (The larger central value and the large uncertainty are due to the fact that the OPP method systematically overestimates barriers far from the lithium ions' reference positions.) Qualitatively, the outcome is clear in both cases: P$_2$ is energetically disfavored and, thus, not part of the migration pattern.

In the TS for Li $\rightleftarrows$ Li$'''$, the migrating lithium ion was octahedrally coordinated at a type-A site with the Li—O distances ranging between 200 and 260 pm. The weaker cation−lithium repulsion along this path led to a lower calculated migration barrier compared to Li $\rightleftarrows$ Li$''$. Its TS structure identifies the lengthy path as Li $\rightleftarrows$ A$'$ $\rightleftarrows$ Li$'''$, which has been excluded from our experimental investigation due to two unfavorable jumps through a LiO$_4$ face under a very acute angle (cf. Table 3).

CONCLUSIONS

Our scrutinous investigations and careful evaluation of hitherto published studies allow us to present a complete, coherent model for lithium-ion diffusion in γ-LiAlO$_2$.

In semiquantitative accordance with computational results, temperature-dependent neutron diffraction showed migration to mainly occur via jumps between lithium positions and adjacent vacancies along a pathway strongly curved in two dimensions (migration barrier: 0.72[5] eV). A longer-range transport first into the channels in [001] (0.87[4] eV), then along them (1.28[13] eV) is possible, but would be less

favored. Both pathways have components along all the principal directions $\langle 100 \rangle$ and [001]. Other hypothetical jumps, which were not examined using diffraction, had been ruled out using straightforward crystal-chemical considerations and rigorous topological analyses.

For different time scales and over a broad temperature range, conductance spectroscopy and the first tracer-diffusion studies on γ-LiAlO$_2$ single-crystals (in (100)- and (001)-orientation, respectively) yielded superimposable solid-state diffusion coefficients/tracer diffusivities and reconcilable activation energies (1.12[1] eV and 1.20[5] eV, respectively). These are comparable to those acquired in former studies on differently oriented single-crystals, being tetragonal and, thus, per se anisotropic. Essentially, the same microscopic process, having components in all principal directions, must be responsible for lithium migration: we attribute it to the direct jump into an adjacent vacancy along the found curved path.

The comparison to measurements on powders suggests that there are two basic possibilities of defect formation as a prerequisite for ion migration. In defect-rich forms like powders, extrinsic activation barriers of 0.7−0.8 eV are found (in good agreement with the migration barrier of 0.72[5] eV from OPP evaluation). Herein, the high abundance of defects with different dimensionalities enables migration without mentionable defect formation barrier. The "intrinsic" activation energy of 1.0−1.2 eV for long-range diffusion, as also present in single crystals, is in fact only *quasi-intrinsic*: Structural defects— e.g., twin boundaries or impurity dopants like iron(II)—are present, albeit in lower concentration. The relatively small formation energy of only 0.48 eV does not allow generating mobile defects from ideal domains, but from preformed structural defects in ample amounts.

ASSOCIATED CONTENT

Ⓢ Supporting Information

The Supporting Information is available free of charge on the ACS Publications website at DOI: 10.1021/acs.chemmater.5b04608.

> Conductivity isotherms, details of crystal structures, neutron diffractograms, and refinement details (PDF)
> Crystallographic information (CIF)
> Crystallographic information (CIF)
> Crystallographic information (CIF)

AUTHOR INFORMATION

Corresponding Author
*Phone: +49 30 314-26178. Fax: +49 30 314-79656. E-mail: dennis.wiedemann@chem.tu-berlin.de (D.W.).

Notes
The authors declare no competing financial interest.

ACKNOWLEDGMENTS

■ REFERENCES

(1) Cao, H.; Xia, B.; Zhang, Y.; Xu, N. LiAlO$_2$-Coated LiCoO$_2$ as Cathode Material for Lithium Ion Batteries. *Solid State Ionics* **2005**, *176*, 911−914.

(2) Li, L.; Chen, Z.; Zhang, Q.; Xu, M.; Zhou, X.; Zhu, H.; Zhang, K. A Hydrolysis-Hydrothermal Route for the Synthesis of Ultrathin LiAlO$_2$-Inlaid LiNi$_{0.5}$Co$_{0.2}$Mn$_{0.3}$O$_2$ as a High-Performance Cathode Material for Lithium Ion Batteries. *J. Mater. Chem. A* **2015**, *3*, 894−904.

(3) Dissanayake, M. A. K. L. Nano-Composite Solid Polymer Electrolytes for Solid State Ionic Devices. *Ionics* **2004**, *10*, 221−225.

(4) Waltereit, P.; Brandt, O.; Trampert, A.; Grahn, H. T.; Menniger, J.; Ramsteiner, M.; Reiche, M.; Ploog, K. H. Nitride Semiconductors Free of Electrostatic Fields for Efficient White Light-Emitting Diodes. *Nature* **2000**, *406*, 865−868.

(5) Takahashi, H.; Yamazaki, N.; Watanabe, T.; Suzuki, K. (Nippon Chemicals Industrial Co.) Gamma Lithium Aluminate Product and Process of Making. U.S. Patent 6,290,928, September 18, 2001.

(6) Rasneur, B. Tritium Breeding Material: γ-LiAlO$_2$. *Fusion Technol.* **1985**, *8*, 1909−1914.

(7) Übeyli, M. Impact of Solid Breeder Materials on Tritium Breeding in a Hybrid Reactor. *J. Fusion Energy* **2006**, *25*, 99−106.

(8) Lei, L.; He, D.; Zou, Y.; Zhang, W.; Wang, Z.; Jiang, M.; Du, M. Phase Transitions of LiAlO$_2$ at High Pressure and High Temperature. *J. Solid State Chem.* **2008**, *181*, 1810−1815.

(9) Marezio, M.; Remeika, J. P. High-Pressure Synthesis and Crystal Structure of α-LiAlO$_2$. *J. Chem. Phys.* **1966**, *44*, 3143−3144.

(10) Bertaut, E. F.; Delapalme, A.; Bassi, G.; Durif-Varambon, A.; Joubert, J.-C. Structure de γ-LiAlO$_2$. *Bull. Soc. Fr. Minéral. Cristallogr.* **1965**, *88*, 103−108.

(11) Marezio, M. The Crystal Structure and Anomalous Dispersion of γ-LiAlO$_2$. *Acta Crystallogr.* **1965**, *19*, 396−400.

(12) Li, X.; Kobayashi, T.; Zhang, F.; Kimoto, K.; Sekine, T. A New High-Pressure Phase of LiAlO$_2$. *J. Solid State Chem.* **2004**, *177*, 1939−1943.

(13) Weyberg, Z. Ueber einige spinellartige Verbindungen. *Centralbl. Mineral., Geol. Paläontol.* **1906**, 645−649.

(14) Hummel, F. A. Thermal Expansion Properties of Some Synthetic Lithia Minerals. *J. Am. Ceram. Soc.* **1951**, *34*, 235−239.

(15) Matsuo, T.; Ohno, H.; Noda, K.; Konishi, S.; Yoshida, H.; Watanabe, H. Nuclear Magnetic Resonance Investigations of Lithium Diffusion in Li2O, Li2SiO3 and LiAlO2. *J. Chem. Soc., Faraday Trans. 2* **1983**, *79*, 1205−1216.

(16) Indris, S.; Heitjans, P.; Uecker, R.; Roling, B. Li Ion Dynamics in a LiAlO$_2$ Single Crystal Studied by ^{7}Li NMR Spectroscopy and Conductivity Measurements. *J. Phys. Chem. C* **2012**, *116*, 14243−14247.

(17) Hu, Q.; Lei, L.; Jiang, X.; Feng, Z. C.; Tang, M.; He, D. Li Ion Diffusion in LiAlO$_2$ Investigated by Raman Spectroscopy. *Solid State Sci.* **2014**, *37*, 103−107.

(18) Wiedemann, D.; Indris, S.; Meven, M.; Pedersen, B.; Boysen, H.; Uecker, R.; Heitjans, P.; Lerch, M. Single-Crystal Neutron Diffraction on γ-LiAlO$_2$: Structure Determination and Estimation of Lithium Diffusion Pathway. *Z. Kristallogr. - Cryst. Mater.* **2015**, DOI: 10.1515/zkri-2015-1896.

(19) Rahn, J.; Witt, E.; Heitjans, P.; Schmidt, H. Lithium Diffusion in Ion-Beam Sputtered Amorphous LiAlO$_2$. *Z. Phys. Chem.* **2015**, *229*, 1341−1350.

(20) Wohlmuth, D.; Epp, V.; Bottke, P.; Hanzu, I.; Bitschnau, B.; Letofsky-Papst, I.; Kriechbaum, M.; Amenitsch, H.; Hofer, F.; Wilkening, M. Order vs. Disorder—A Huge Increase in Ionic Conductivity of Nanocrystalline LiAlO$_2$ Embedded in an Amorphous-Like Matrix of Lithium Aluminate. *J. Mater. Chem. A* **2014**, *2*, 20295−20306.

(21) Islam, M. M.; Bredow, T. Interstitial Lithium Diffusion Pathways in γ-LiAlO$_2$: A Computational Study. *J. Phys. Chem. Lett.* **2015**, *6*, 4622−4626.

(22) Jacobs, J.-P.; San Miguel, M. A.; Alvarez, L. J.; Giral, P. B. Lithium Diffusion in γ-LiAlO$_2$, a Molecular Dynamics Simulation. *J. Nucl. Mater.* **1996**, *232*, 131−137.

(23) Konishi, S.; Ohno, H. Electrical Conductivity of Polycrystalline Li$_2$SiO$_3$ and γ-LiAlO$_2$. *J. Am. Ceram. Soc.* **1984**, *67*, 418−419.

(24) Witt, E.; Nakhal, S.; Chandran, C. V.; Lerch, M.; Heitjans, P. NMR and Impedance Spectroscopy Studies on Lithium Ion Diffusion in Microcrystalline γ-LiAlO$_2$. *Z. Phys. Chem.* **2015**, *229*, 1327−1339.

(25) Indris, S.; Uecker, R.; Heitjans, P. Li Diffusion in LiAlO$_2$ Single Crystals Studied with NMR Spectroscopy. *Diffus. Fundam.* **2005**, *2*, 50-1−50-2.

(26) Langer, J.; Wohlmuth, D.; Kovalcik, A.; Epp, V.; Stelzer, F.; Wilkening, M. Mechanical Detection of Ultraslow, Debye-Like Li-Ion Motions in LiAlO$_2$ Single Crystals. *Ann. Phys. (Berlin, Ger.)* **2015**, *527*, 523−530.

(27) Bergerhoff, G.; Brown, I. D. Inorganic Crystal Structure Database. In *Crystallographic Databases*; Allen, F. H., Bergerhoff, G., Sievers, R., Eds.; International Union of Crystallography: Chester, U.K., 1987; Chapter 2.2, pp 77−95.

(28) Petříček, V.; Dušek, M.; Palatinus, L. Crystallographic Computing System JANA2006: General Features. *Z. Kristallogr. - Cryst. Mater.* **2014**, *229*, 345−352.

(29) Thompson, P.; Cox, D. E.; Hastings, J. B. Rietveld Refinement of Debye-Scherrer Synchrotron X-Ray Data from Al$_2$O$_3$. *J. Appl. Crystallogr.* **1987**, *20*, 79−83.

(30) Bérar, J.-F.; Baldinozzi, G. Modeling of Line-Shape Asymmetry in Powder Diffraction. *J. Appl. Crystallogr.* **1993**, *26*, 128−129.

(31) Brandenburg, K.; Putz, H. *Diamond*, version 3.2; Crystal and Molecular Structure Visualization; Crystal Impact: Bonn (Germany), 2014.

(32) Wolff, S. K.; Grimwood, D. J.; McKinnon, J. J.; Turner, M. J.; Jayatilaka, D.; Spackman, M. A. *CrystalExplorer*, version 3.1; Crystal Structure Analysis with Hirshfeld Surfaces; University of Western Australia: Perth (Australia), 2012.

(33) Blatov, V. A.; Shevchenko, A. P.; Proserpio, D. M. Applied Topological Analysis of Crystal Structures with the Program Package ToposPro. *Cryst. Growth Des.* **2014**, *14*, 3576−3586.

(34) Blatov, V. A.; Ilyushin, G. D.; Blatova, O. A.; Anurova, N. A.; Ivanov-Schits, A. K.; Dem'yanets, L. N. Analysis of Migration Paths in Fast-Ion Conductors with Voronoi-Dirichlet Partition. *Acta Crystallogr., Sect. B: Struct. Sci.* **2006**, *62*, 1010−1018.

(35) Kuhs, W. Generalized Atomic Displacements in Crystallographic Structure Analysis. *Acta Crystallogr., Sect. A: Found. Crystallogr.* **1992**, *48*, 80−98.

(36) Wiedemann, D. *CalcOPP*, version 1.6.1; Calculation of 2D OPP from PDF Data; Technische Universität Berlin: Berlin (Germany), 2015, DOI: 10.6084/m9.figshare.1461721.

(37) Momma, K.; Izumi, F. *VESTA 3* for Three-Dimensional Visualization of Crystal, Volumetric and Morphology Data. *J. Appl. Crystallogr.* **2011**, *44*, 1272−1276.

(38) OriginLab. *OriginPro*, version 2015; Data Analysis and Graphing Software; OriginLab Corp.: Northampton, U.S.A., 2015.

(39) Crank, J. *The Mathematics of Diffusion*; Oxford University Press: Oxford, U.K., 1975.

(40) Heitjans, P.; Schirmer, A.; Indris, S. NMR and β-NMR Studies of Diffusion in Interface-Dominated and Disordered Solids. In *Diffusion in Condensed Matter*; Heitjans, P., Kärger, J., Eds.; Springer: Berlin, Germany, 2005; Chapter 9, pp 367−415. DOI: 10.1007/3-540-30970-5_9.

(41) Andrew, E. R. Developments in the Motional Narrowing of the NMR Spectra of Solids—Microscopic and Macroscopic. *Pure Appl. Chem.* **1972**, *32*, 41−51.

(42) Wilkening, M.; Bork, D.; Indris, S.; Heitjans, P. Diffusion in Amorphous LiNbO$_3$ Studied by ^{7}Li NMR — Comparison with the Nano- and Microcrystalline Material. *Phys. Chem. Chem. Phys.* **2002**, *4*, 3246−3251.

(43) Filsø, M. Ø.; Turner, M. J.; Gibbs, G. V.; Adams, S.; Spackman, M. A.; Iversen, B. B. Visualizing Lithium-Ion Migration Pathways in Battery Materials. *Chem. - Eur. J.* **2013**, *19*, 15535−15544.

(44) Shannon, R. D. Revised Effective Ionic Radii and Systematic Studies of Interatomic Distances in Halides and Chalcogenides. *Acta Crystallogr., Sect. A: Cryst. Phys., Diffr., Theor. Gen. Crystallogr.* **1976**, *32*, 751−767.

(45) Trueblood, K. N.; Bürgi, H.-B.; Burzlaff, H.; Dunitz, J. D.; Gramaccioli, C. M.; Schulz, H. H.; Shmueli, U.; Abrahams, S. C. Atomic Displacement Parameter Nomenclature. Report of a Subcommittee on Atomic Displacement Parameter Nomenclature. *Acta Crystallogr., Sect. A: Found. Crystallogr.* **1996**, *52*, 770−781.

(46) Boysen, H. The Determination of Anharmonic Probability Densities from Static and Dynamic Disorder by Neutron Powder Diffraction. *Z. Kristallogr. - Cryst. Mater.* **2003**, *218*, 123−131.

(47) Chadwick, A. V.; Flack, K. W.; Strange, J. H.; Harding, J. Defect Structures and Ionic Transport in Lithium Oxide. *Solid State Ionics* **1988**, *28−30* (1), 185−188.

(48) Chou, M. M. C.; Chun Tsao, P.; Chun Huang, H. Study on Czochralski Growth and Defects of $LiAlO_2$ Single Crystals. *J. Cryst. Growth* **2006**, *292*, 542−545.

(49) Chou, M. M. C.; Huang, H. C.; Gan, D.-S.; Hsu, C. W. C. Defect Characterizations of γ-$LiAlO_2$ Single Crystals. *J. Cryst. Growth* **2006**, *291*, 485−490.

(50) Nie, A.; Gan, L.-Y.; Cheng, Y.; Li, Q.; Yuan, Y.; Mashayek, F.; Wang, H.; Klie, R.; Schwingenschlogl, U.; Shahbazian-Yassar, R. Twin Boundary-Assisted Lithium Ion Transport. *Nano Lett.* **2015**, *15*, 610−615.

(51) Moriwake, H.; Kuwabara, A.; Fisher, C. A. J.; Huang, R.; Hitosugi, T.; Ikuhara, Y. H.; Oki, H.; Ikuhara, Y. First-Principles Calculations of Lithium-Ion Migration at a Coherent Grain Boundary in a Cathode Material, $LiCoO_2$. *Adv. Mater.* **2013**, *25*, 618−622.

(52) Holston, M. S.; McClory, J. W.; Giles, N. C.; Halliburton, L. E. Radiation-Induced Defects in $LiAlO_2$ Crystals: Holes Trapped by Lithium Vacancies and Their Role in Thermoluminescence. *J. Lumin.* **2015**, *160*, 43−49.

(53) Grimme, S.; Ehrlich, S.; Goerigk, L. Effect of the Damping Function in Dispersion Corrected Density Functional Theory. *J. Comput. Chem.* **2011**, *32*, 1456−1465.